Plasmon coupling in extended structures: Graphene superlattice nanoribbon arrays

Daniel Rodrigo,[1,*] Tony Low,[2] Damon B. Farmer,[3] Hatice Altug,[1] and Phaedon Avouris[3,†]
[1]*Institute of Bioengineering, École Polytechnique Fédérale de Lausanne (EPFL), Lausanne 1015, Switzerland*
[2]*Department of Electrical & Computer Engineering, University of Minnesota, Minneapolis, Minnesota 55455, USA*
[3]*IBM Research Division, T.J. Watson Research Center, Yorktown Heights, New York 10598, USA*
(Received 16 November 2015; revised manuscript received 16 February 2016; published 4 March 2016)

Interaction between localized plasmons in isolated proximal nanostructures is a well-studied phenomenon. Here we explore plasmon-plasmon interactions in connected extended systems. Such systems can now be easily produced experimentally using graphene. However, the mechanisms of plasmonic interactions in extended systems are not well understood. We employ finite-element methods to study these interactions in graphene superlattice nanoribbon arrays with a periodically modulated electrochemical potential or number of layers. We find a rich variation in the resulting plasmonic resonances depending on the dimensions, the electrochemical potentials (doping), and the separation of the nanoribbon segments, and we demonstrate the involvement of both transverse and longitudinal plasmon-plasmon interactions. For example, unlike predictions based on the well-known "orbital hybridization model," the energies of the resulting hybrid plasmonic resonances in the extended system can lie between the energies of the plasmons in the individual components. Our results demonstrate that the plasmonic spectra of graphene superlattice structures can be easily adjusted, continuously tuned, and used to enhance optical fields in the infrared and terahertz regions of the electromagnetic spectrum.

DOI: 10.1103/PhysRevB.93.125407

I. INTRODUCTION

Plasmonics is a well-developed and active field. It is based primarily on noble and coin metals, namely Au, Ag, and Cu. The excitation of localized plasmons in micro- and nanostructures made of these materials is used extensively to enhance linear and nonlinear optical phenomena in the visible and near-infrared sections of the electromagnetic (EM) spectrum [1–4]. Graphene is a semimetal with properties that can further extend the plethora of phenomena and applications of plasmonics. Specifically, unlike conventional metals, the carrier density of graphene structures, and therefore their plasmonic resonances, are tunable by electrostatic or chemical doping over a wide range: 10^{11}-10^{14} carriers/cm^2 [5,6]. Because it is a two-dimensional (2D) material, graphene can easily be patterned using the well-developed planar patterning techniques of the semiconductor industry to generate new types of ultrathin and flexible plasmonic structures [7–10]. Due to the very high mobility of carriers in graphene, plasmons at low energies can be long-lived and have strong confinement factors ($\lambda_{vac}/\lambda_{graphene} \approx 100$) and large Purcell factors (10^6–$10^7\lambda_0^{-3}$) [11–13]. Finally, the resonance frequencies of graphene nano- and microstructures cover the mid-infrared, far-infrared, and terahertz sections of the spectrum and thus supplement and extend noble metal plasmonics [14–17].

Interactions between nearby localized plasmons of metallic particles and the resonances of complex shaped structures are typically described very successfully by the *orbital hybridization* model [2,18–21]. In analogy with the interaction of atomic orbitals between two atoms that generate bonding and antibonding states, plasmonic resonances below and above the isolated resonances should result. This model has also been applied successfully to simple graphene plasmonic structures such as graphene rings [22] and dots [23]. However, the application of planar fabrication technology to graphene allows the generation of extended graphene structures with increased complexity. Understanding plasmonic interactions in such systems would allow the design of structures with prescribed plasmonic spectra. One such structure was recently studied experimentally [24]. It consists of a continuous single-layer graphene nanoribbon array (GNRA) periodically overlaid with segments of a second graphene layer [Fig. 1(a)] [24]. It was found that application of the simple form of the orbital hybridization model could not account for the resulting plasmonic resonances. In this work, we use this structure as an example to explore the nature of the plasmonic interactions in extended graphene structures typically referred to as a superlattice array [25]. We investigate first graphene nanoribbon arrays where the chemical potential is periodically modulated having alternating segments of, respectively, low and high chemical potential [Fig. 1(b)]. Next, we explore graphene superlattice arrays where graphene nanoribbons alternate segments with a different number of layers [Fig. 1(a)]. We show the connection between these two structures and analyze the nature of the new plasmonic modes supported by these novel graphene structures.

II. GNRAs WITH ALTERNATING CHEMICAL POTENTIAL

A typical extinction coefficient of the GNRA with alternating chemical potential is shown in Fig. 2(a). The simulations are performed solving the Maxwell equations with a 3D finite-element method. Graphene is modeled as a two-dimensional surface with Drude conductivity. A detailed description of the simulation approach is provided in Appendix A. In this figure, we represent the extinction coefficient when the chemical potential of section 1 is kept constant ($\mu_{c1} = 0.35$ eV) and the potential of section 2 is varied (μ_{c2}). The structure parameters considered, unless stated otherwise, are a ribbon

*daniel.rodrigo@epfl.ch
†avouris@us.ibm.com

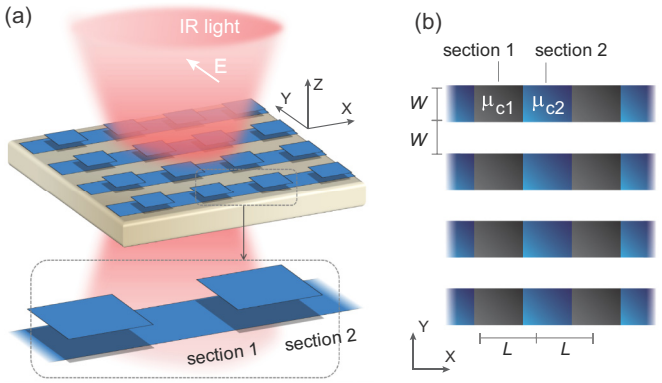

FIG. 1. (a) Conceptual view of the graphene nanoribbon array (GNRA) with an alternating number of layers. Each nanoribbon alternates sections of single-layer (section 1) and double-layer (section 2) graphene. The plasmonic excitation is performed by infrared light illumination polarized transversally to the nanoribbons. (b) GNRA with a modulated chemical potential. Each nanoribbon alternates sections of low chemical potential (μ_{c1} in section 1) and high chemical potential (μ_{c2} in section 2).

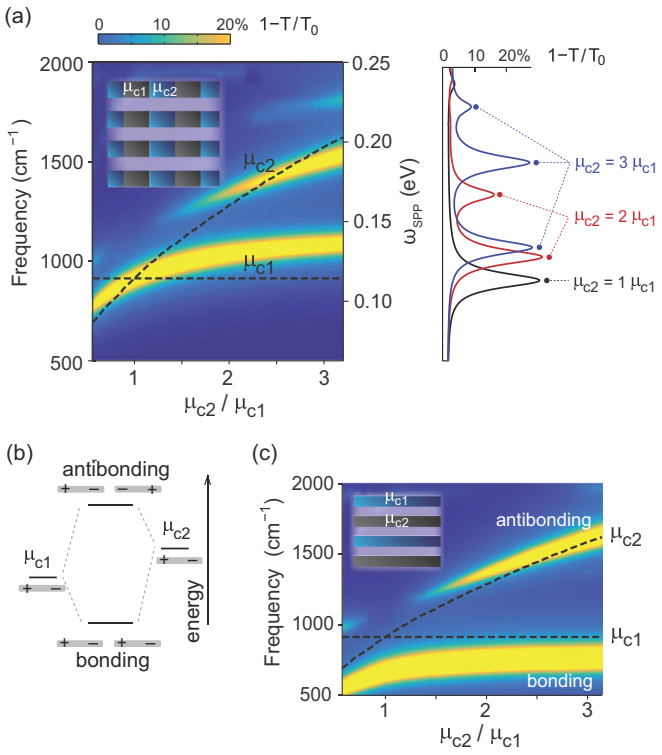

FIG. 2. (a) Extinction coefficient ($1 - T/T_0$) of the GNRA with alternating chemical potential ($W = L = 100$ nm, $\mu_{c1} = 0.35$ eV, $\tau = 70$ fs). T and T_0 are the transmission coefficients with and without graphene nanoribbons, respectively. Dashed lines represent the resonance frequency of GNRAs with uniform potential μ_{c1} and μ_{c2}. (b) Schematic description of the orbital hybridization model, showing the energies of the bonding and antibonding hybridized modes. (c) Extinction coefficient of a GNRA with uniform potential nanoribbons where adjacent ribbons in close proximity alternate between μ_{c1} and μ_{c2}. The distance between adjacent nanoribbons is $W/20 = 5$ nm.

width and section length $W = L = 100$ nm, and graphene at room temperature with chemical potential $\mu_{c1} = 0.35$ eV and relaxation time $\tau = 70$ fs. The graphene parameters are in the same range as those obtained from experimental data for nanopatterned CVD graphene [26]. The calculated resonance frequencies of GNRAs with a uniform chemical potential μ_{c1} and μ_{c2} are represented with respective dashed lines that follow the theoretical dependence ($\omega_{SPP} \sim \sqrt{\mu_c}$) [7]. We observe that the single resonance of the uniform GNRA ($\mu_{c2} = \mu_{c1}$) is transformed into a multiresonance response when $\mu_{c2} \neq \mu_{c1}$. A first low-energy mode is spectrally located between the resonances of μ_{c1} and μ_{c2} uniform-potential GNRAs (dashed lines). A second mode is located either below or above the μ_{c2} resonance depending on the parameters, and in some cases a third mode can appear (for instance, for $\mu_{c2} = 3\mu_{c1}$). This response cannot be directly described using the orbital hybridization model [Fig. 2(b)], which predicts bonding and antibonding modes producing resonances, respectively, located below and above the individual resonance frequencies for μ_{c1} and μ_{c2}. However, the orbital hybridization model can successfully describe the case in which each nanoribbon has a uniform potential and adjacent nanoribbons in close proximity alternate between μ_{c1} and μ_{c2} [Fig. 2(c)]. While this second structure shows clearly a bonding and antibonding mode, further description beyond orbital hybridization is needed for the nanoribbon superlattice.

The plasmonic nature of the superlattice GNRA is strongly determined by the length L of the sections with alternating potential [27]. When sections are much shorter than the plasmon wavelength ($L \ll \lambda_{SPP}$ or equivalently $L \ll W$), variations in the chemical potential are produced at a much smaller scale than the plasmon wavelength, and, as a result, graphene behaves as a uniform effective medium [Fig. 3(a)]. These short-section structures, therefore, operate as uniform-potential GNRAs with an average chemical potential between μ_{c1} and μ_{c2}, producing a single resonance located between those of uniform μ_{c1} and μ_{c2} GNRAs, respectively. On the other hand, when sections are much longer than the plasmon wavelength ($L \gg \lambda_{SPP}$ or equivalently $L \gg W$), the two sections support independent plasmonic resonances [Fig. 3(b)]. As a result, the long-section structures behave as two independent GNRAs with uniform potential μ_{c1} and μ_{c2} producing two separate resonances matching those of the uniform GNRAs. The transition from short to long sections is explored in Fig. 3(c) for a varying length L and $\mu_{c2} = 2\mu_{c1}$. While the two extreme cases for the section length ($L \ll \lambda_{SPP}$ and $L \gg \lambda_{SPP}$) produce plasmonic behavior of uniform-potential GNRAs, the transition cases between short and long sections ($L \approx \lambda_{SPP}$) show additional resonance peaks that require further study.

To understand the nature of the new modes arising when the section length is comparable to the plasmon wavelength, we study the charge distribution and dispersion of these modes for a varying plasmonic wave vector q by changing the nanoribbon width W (Fig. 4). The dashed lines show the simulated resonance frequencies of uniform-potential nanoribbons at μ_{c1} and μ_{c2}, which follow the theoretical dispersion for graphene plasmons $\omega_{SPP} \sim 1/\sqrt{W}$. To be more precise, the dispersion of graphene plasmons is $q = \pi/W = \frac{\hbar^2 \pi \epsilon_0 (1+\epsilon_r)}{e^2 \mu_c} \omega_{SPP}^2$ [9].

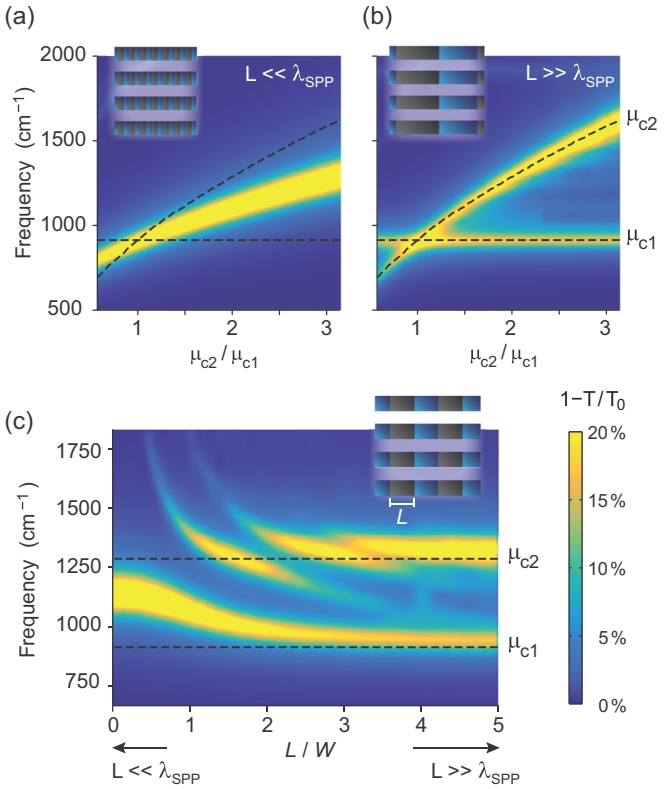

FIG. 3. (a) Extinction coefficient of the GNRA with alternating chemical potential for a section length L much shorter than the plasmon wavelength ($L = W/5 = 20$ nm) and (b) much longer than the plasmon wavelength ($L = 5W = 500$ nm). Dashed lines represent the resonance frequency of uniform-potential GNRAs. (c) Extinction for a section length L covering the transition between short and long sections ($\mu_{c2} = 2\mu_{c1} = 0.7$ eV).

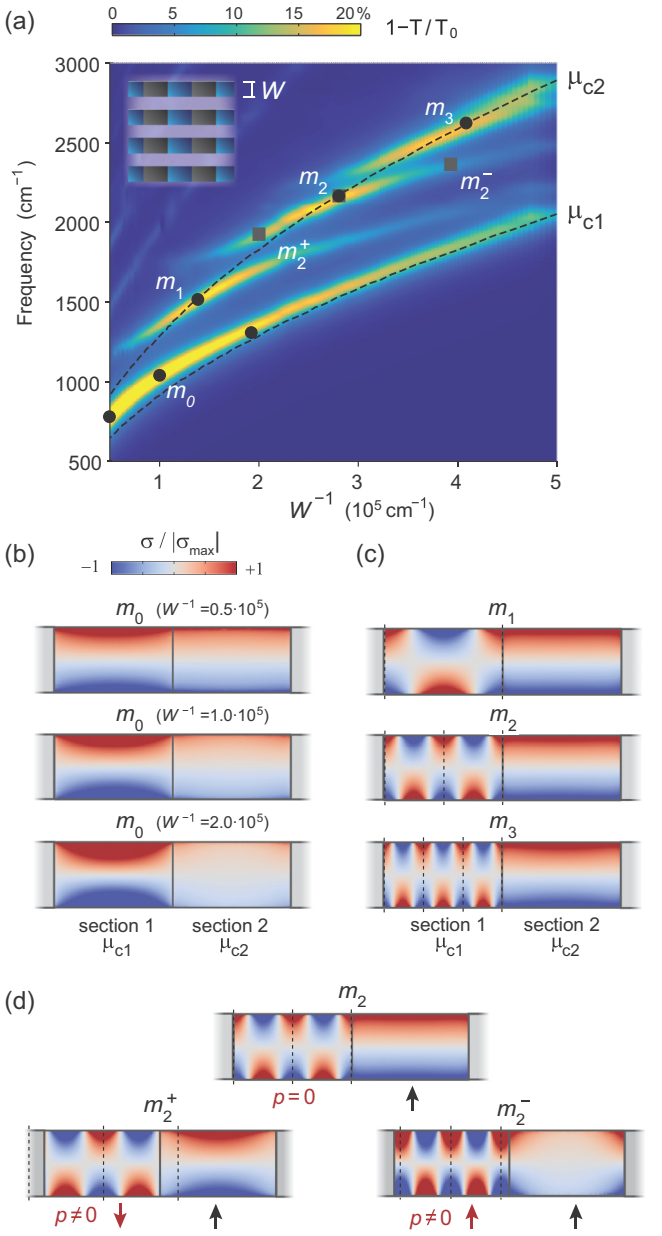

FIG. 4. (a) Dispersion of the plasmonic modes supported by the alternating chemical potential GNRA ($L = 100$ nm, $\mu_{c2} = 2\mu_{c1} = 0.7$ eV). (b)–(d) Electrical charge density distribution σ for each mode (m_0, m_1, m_2, and m_3). The corresponding frequency and wave vector for each charge distribution are indicated with corresponding markers in the dispersion plot. The arrows in (d) indicate the sign of the total dipolar moment p of each section.

We see that the interaction leads to two branches in the dispersion curve of the system [Fig. 4(a)]. The low-frequency mode labeled m_0 is continuous and its energy lies overall above the energy of the μ_{c1} graphene dispersion (lower dashed curve). The other branch is discontinuous showing a number of gaps. Some points, labeled m_1,m_2,m_3, . . . , lie on top of the dispersion of the μ_{c2} graphene (upper dashed line), while others lie below (m_2^-) or above (m_2^+) that dispersion curve. To understand the physical origin of this behavior, we plot the electric charge distribution for each mode. We observe that for all modes, the field over section 2 (higher chemical potential μ_{c2}) represents a charge separation (dipole formation) as expected from the excitation of the fundamental plasmonic mode, although variations in the spatial distribution of charges can be seen. Over section 1 (lower chemical potential μ_{c1}), an increasing number of longitudinal field oscillations is observed. The origin of the oscillations can be understood by considering the radii of the plasmon isoenergy surfaces of regions 1 and 2. Region 1 has a lower chemical potential than region 2 ($\mu_{c1} < \mu_{c2}$). Now the plasmon wave vector in graphene is given by $q \approx \hbar\omega^2/(2\alpha_0\mu_c c) \sim 1/\sqrt{\eta}$, where α_0 is the fine-structure constant and η is the free carrier density [7,10]. Thus the isoenergy surface radius of section 1 is larger than that of section 2, i.e., it contains a larger number of wave vectors. In the higher doped section 2, the transverse momentum imparted by the finite ribbon width, $q_y \approx 3\pi/4W$ [28], lies along the isoenergy contour and is excited when it is in resonance with the incident light. Plasmon waves with the extra wave vectors in section 1 cannot propagate 1 into section 2. This effect can be seen in Fig. 4(b), which gives the charge distribution of mode m_0. We observe that for high wave numbers the charge is essentially localized on segment 1, while for low wave numbers it is spread on both segments. As a consequence, the resonance of mode m_0 overlaps that of a μ_{c1} uniform-potential GNRA, except for the lowest

wave vectors, whose resonance is located between the μ_{c1} and μ_{c2} resonances. The nonpropagating wave vectors from segment 1 are reflected at the boundary with segment 2 and form standing waves within region 1 akin to Fabry-Pérot-type oscillations [29] [Fig. 4(c)]. Depending on the size of section 1, an even or odd number of plasmon half-wavelengths can be accommodated. When an even number fits in section 1, then the dipole moment p of this segment vanishes, there is minimal interaction between segments, the energies of modes $m_1, m_2, m_3, \ldots$ lie on top of the double-layer dispersion, and the charge distribution becomes uniform along section 2. On the other hand, when an odd number of half-wavelengths is present, then a dipole is formed in region 1, which can be parallel or antiparallel to that of the dipole of section 2, thus leading to modes higher (m_2^+) or lower in energy (m_2^-), respectively [Fig. 4(d)]. Since the dipole p of section 1 flips its direction when the mode number increases by 1, this results in the formation of gaps in the dispersion.

We also note here that these results are not significantly modified when we allow for a smooth transition between μ_{c1} and μ_{c2} (Fig. 5). This indicates that the new modes supported by the alternating potential GNRA are created by the periodic modulation of the chemical potential rather than by an abrupt discontinuity between sections.

To further understand the physics of the alternating potential GNRA, we extend the dispersion analysis to different chemical potentials μ_{c2} [Fig. 6(a)]. We observe that for the different values of μ_{c2}, the modes $m_1, m_2, m_3, \ldots$ are rescaled along the horizontal axis to follow the shift of the resonance corresponding to a uniform μ_{c2} GNRA (top dashed line). On the other hand, there is no variation in the range of allowed frequencies for these modes (i.e., no variation in the vertical scale). Indeed, these allowed frequencies are controlled by the standing wave created along section 1, and they depend in particular on the section length L as shown in Fig. 6(b). As the section length L is increased, the modes $m_1, m_2, m_3, \ldots$

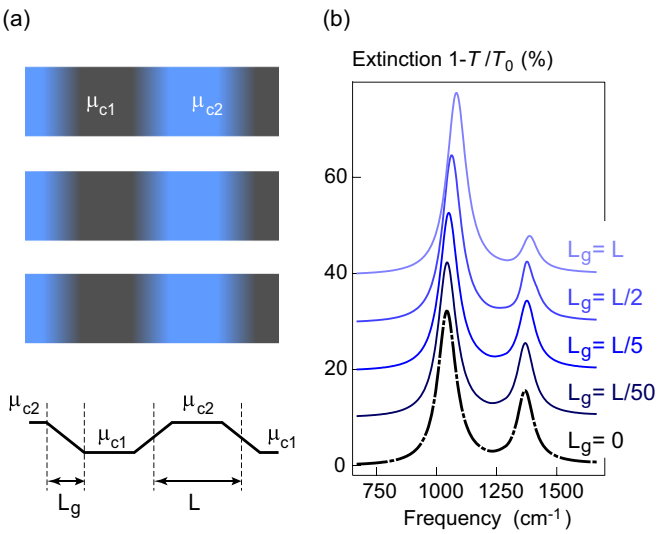

FIG. 5. (a) Alternating chemical potential GNRA with a smooth transition between sections. The chemical potential is linearly tapered over a transition region of length L_g. (b) Extinction spectra for different transition lengths L_g.

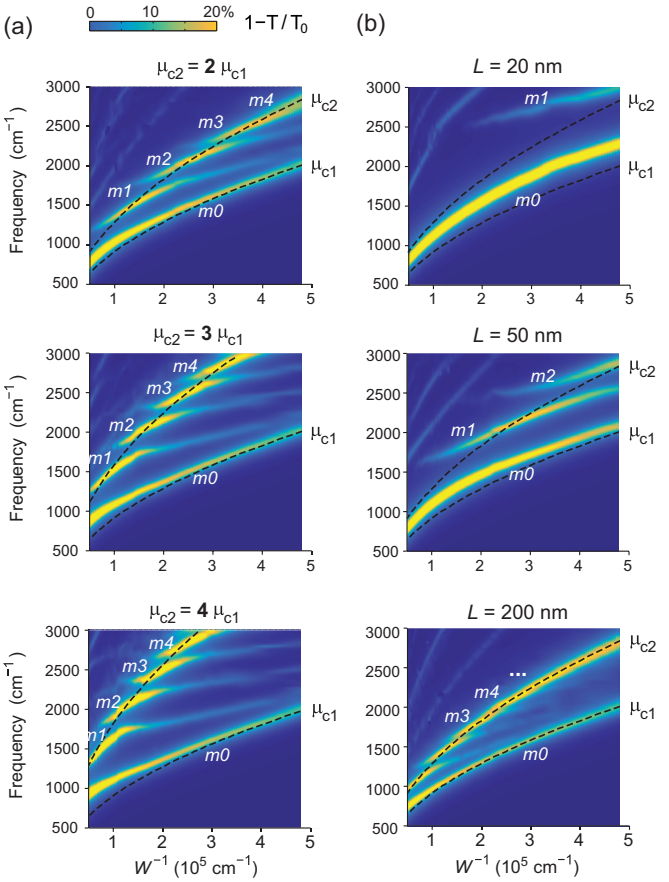

FIG. 6. Dispersion of the plasmonic modes of the alternating chemical potential GNRA for (a) increasing values of chemical potential in section 2 and (b) different section lengths L.

are excited at lower frequencies. This is evidenced in Fig. 6(b) as a vertical rescaling along the frequency axis. We observe that for short lengths, only mode m_0 is active and is located in between the resonances of μ_{c1} and μ_{c2} uniform-potential GNRAs (dashed lines). As L is progressively increased, modes $m_1, m_2, m_3, \ldots$ are excited at lower frequencies and provide additional resonance peaks. Finally, for long lengths, we see that modes $m_1, m_2, m_3, \ldots$ group together along the μ_{c2} resonance dashed line, while mode m_0 overlaps with the μ_{c1} resonance dashed line. These observations provide an explanation for the multiple peaks shown first in Fig. 2, and they give a complete description of the transition between the single resonance of short sections ($L \ll \lambda_{SPP}$) and the double resonance of long sections ($L \gg \lambda_{SPP}$) initially shown in Fig. 3.

III. GNRAs WITH AN ALTERNATING NUMBER OF LAYERS

We investigate next the graphene superlattice array where nanoribbons are divided into sections alternating between single-layer and double-layer graphene. The double-layer region is composed of two identical layers separated by an interlayer distance g. The extinction spectra of the GNRA for different values of g are shown in Figs. 7(a) and 7(b). In our model we assume negligible interlayer tunneling, which

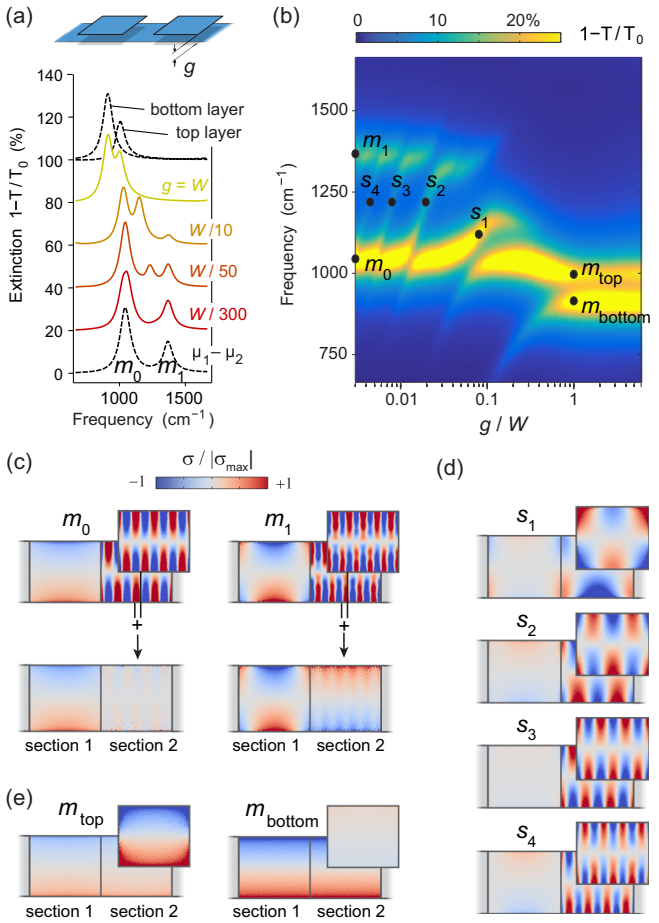

FIG. 7. (a), (b) Extinction spectrum of the GNRA with alternating single-layer and double-layer graphene sections ($W = L = 100$ nm). The two-layer section is considered to be two identical graphene layers ($\mu_c = 0.35$ eV) separated by an air gap with thickness g. Dashed lines correspond to the spectrum of the alternating chemical potential model ($\mu_{c2} = 2\mu_{c1} = 0.7$ eV) and isolated top/bottom layers. (c)–(e) Electrical charge-density distribution for each mode at the frequency and gap g indicated in the extinction plot. The bottom plots in (c) represent the addition of the charges in the top and bottom layers.

is the case for graphene layers with random stacking [30,31]. We observe that for the smallest gap, the extinction spectrum is in excellent agreement with that of the alternating chemical potential model ($\mu_{c1} - \mu_{c2}$). This is due to the strong coupling between the plasmons in the two layers when $g \ll \lambda_{SPP}$ [16]. More generally, a stack of graphene layers separated by infinitesimal spacing is electromagnetically equivalent to a single layer incorporating the conductivities of the individual layers. The added conductivity of parallel graphene layers with Drude conductivity is

$$\sigma_{eq} = \sum_j \sigma_j = \sum_j \frac{ie^2}{\hbar\pi} \frac{\mu_c^{(j)}}{\omega + i/\tau}$$

[32], where $\mu_c^{(j)}$ is the chemical potential of each layer. Then, we can replace multilayer graphene by single-layer graphene with an equivalent chemical potential $\mu_{c,eq} = \sum_j \mu_c^{(j)}$. As a result, the structures with alternating chemical potential and an alternating number of layers are equivalent when the interlayer distance g tends to zero.

As the gap g increases, the coupling between layers weakens and we observe additional plasmonic resonances [s_1,s_2,s_3, . . . in Fig. 7(b)] that were not initially observed using the alternating chemical potential model. The origin of these resonances can be determined by observing their corresponding charge-density distributions. The charge density for modes m_0 and m_1 [Fig. 7(c)] shows a high-order Fabry-Pérot resonance coupled over the double-layer section (section 2) with opposite charge polarity for each layer. When the charges on the top and bottom layers are added, the high-order Fabry-Pérot oscillation vanishes, leaving only the symmetric component of the charge distribution, which is identical to that initially obtained from the $\mu_{c1} - \mu_{c2}$ model. As shown in Fig. 7(d), the multiple orders of the antisymmetric Fabry-Pérot oscillations on the double-layer section create the additional resonances s_1,s_2,s_3, . . . , which were not present in the single-layer model. Finally, when the gap distance becomes comparable to or larger than the plasmon wavelength (e.g., $g = W$), the two layers become uncoupled and generate two resonances (m_{bottom} and m_{top}) independently produced by the bottom and top layer [Fig. 7(e)]. In summary, the multilayer superlattice is equivalent to the alternating potential structure for $g = 0$ due to the strong coupling between plasmons in the two layers. This coupling becomes progressively weakened as g increases, and the plasmonic response of the multilayer superlattice shows new resonances converging toward the response of two isolated graphene layers.

IV. CONCLUSION

The results presented above demonstrate that graphene superlattice nanostructures that combine sections with multiple layers or different dopings provide great versatility to tailor the plasmonic response beyond that of canonical structures such as nanoribbons or nanodots. These simulations reveal the nature of the new plasmonic modes arising in these superlattice arrays, and they provide a guide to adjust the number of resonances in the structure, as well as their spectral position. As our ability to fabricate increasingly complex multilayer devices improves and the number of available two-dimensional materials increases, our understanding of plasmonic modes in compound structures will ultimately enable us to engineer the plasmonic resonance response of two-dimensional nanostructures.

ACKNOWLEDGMENT

This work was funded in part by the European Commission (FP7-IEF-2013-625673-GRYPHON) and the Swiss National Science Foundation (SNSF) through project 133583.

APPENDIX: COMPUTATIONAL DETAILS

The simulations are carried out calculating the full 3D electromagnetic field in the structure by using the finite-elements method (Ansys HFSS v15 software) to solve Maxwell equations in the frequency domain. The simulated

structure consists of a three-dimensional unit cell arranged in a two-dimensional periodic array. The electromagnetic excitation consists of a plane wave with an orthogonal incidence angle and polarization transverse to the graphene nanoribbons. Graphene is modeled as a zero-thickness two-dimensional surface enforcing an impedance boundary condition where the ratio between tangential components of the electric and magnetic fields is equal to graphene conductivity. Graphene surface conductivity is calculated using the Drude model as

$$\sigma = \frac{ie^2}{\hbar\pi}\frac{\mu_c}{\omega + i/\tau}$$

[32], including the temperature effect ($T = 300$ K) as

$$\mu_c = \mu_{c,0} + 2k_B T \ln(1 + e^{-\mu_{c,0}/k_B T}).$$

The relaxation time for nanopatterned CVD graphene is $\tau = 70$ fs in accordance with experimental data [26]. Graphene is supported by a dielectric substrate with refractive index $n_s = 1.4$, and the interlayer volume in the double-layer model has refractive index $n_{2L} = 1$. The structure periodicity is defined by two pairs of Floquet-Bloch periodic boundary conditions on the surfaces delimiting the unit cell. We use an initial mesh with tetrahedral elements having a maximum length of $W/15$. The mesh is iteratively refined by increasing the number of mesh elements by 30% each iteration. The convergence criterion is defined as $|t^N - t^{N-1}| < 0.02$, where t is the complex transmission coefficient and N is the iteration number. The electric surface charge density (q_s) is calculated from the charge-conservation equation as $q_s = -\nabla J_s$, where J_s is the surface current in graphene. Experimental validation of the computational technique for graphene nanoribbon arrays can be found in Ref. [17].

[1] S. Maier, *Plasmonics: Fundamentals and Applications* (Springer, New York, 2007).
[2] N. J. Halas, S. Lal, W. S. Chang, S. Link, and P. Nordlander, Chem. Rev. **111**, 3913 (2011).
[3] H. A. Atwater and A. Polman, Nat. Mater. **9**, 205 (2010).
[4] M. Kauranen and A. V. Zayats, Nat. Photon **6**, 737 (2012).
[5] V. W. Brar, M. S. Jang, M. Sherrott, J. J. Lopez, and H. A. Atwater, Nano Lett. **13**, 2541 (2013).
[6] F. J. Garcia de Abajo, ACS Photon. **1**, 135 (2014).
[7] A. N. Grigorenko, M. Polini, and K. S. Novoselov, Nat. Photon **6**, 749 (2012).
[8] F. H. L. Koppens, D. E. Chang, and F. J. Garcia de Abajo, Nano Lett. **11**, 3370 (2011).
[9] M. Jablan, H. Buljan, and M. Soljacic, Phys. Rev. B **80**, 245435 (2009).
[10] T. Low and P. Avouris, ACS Nano **8**, 1086 (2014).
[11] J. Chen, M. Badioli, P. Alonso-González, S. Thongrattanasiri, F. Huth, J. Osmond, M. Spasenović, A. Centeno, A. Pesquera, P. Godignon, A. Zurutuza Elorza, N. Camara, F. J. Garcia de Abajo, R. Hillenbrand, and F. H. L. Koppens, Nature (London) **487**, 77 (2012).
[12] Z. Fei, A. S. Rodin, G. O. Andreev, W. Bao, A. S. McLeod, M. Wagner, L. M. Zhang, Z. Zhao, M. Thiemens, G. Dominguez, M. M. Fogler, A. H. Castro Neto, C. N. Lau, F. Keilmann, and D. N. Basov, Nature (London) **487**, 82 (2012).
[13] A. Woessner, M. B. Lundeberg, Y. Gao, A. Principi, P. Alonso-Gonzalez, M. Carrega, K. Watanabe, T. Taniguchi, G. Vignale, M. Polini, J. Hone, R. Hillenbrand, and F. H. L. Koppens, Nat. Mater. **14**, 421 (2015).
[14] Y. Li, H. Yan, D. B. Farmer, X. Meng, W. Zhu, R. M. Osgood, T. F. Heinz, and P. Avouris, Nano Lett. **14**, 1573 (2014).
[15] L. Ju, B. Geng, J. Horng, C. Girit, M. Martin, Z. Hao, H. A. Bechtel, X. Liang, A. Zettl, and Y. R. Shen, Nat. Nano **6**, 630 (2011).
[16] H. Yan, X. Li, B. Chandra, G. Tulevski, Y. Wu, M. Freitag, W. Zhu, P. Avouris, and F. Xia, Nat. Nano **7**, 330 (2012).
[17] D. Rodrigo, O. Limaj, D. Janner, D. Etezadi, F. J. Garcia de Abajo, V. Pruneri, and H. Altug, Science **349**, 165 (2015).
[18] E. Prodan, C. Radloff, N. J. Halas, and P. Nordlander, Science **302**, 419 (2003).
[19] E. Prodan and P. Nordlander, J. Chem. Phys. **120**, 5444 (2004).
[20] S. Sheikholeslami, Y.-w. Jun, P. K. Jain, and A. P. Alivisatos, Nano Lett. **10**, 2655 (2010).
[21] P. K. Jain, S. Eustis, and M. A. El-Sayed, J. Phys. Chem. B **110**, 18243 (2006).
[22] Z. Fang, S. Thongrattanasiri, A. Schlather, Z. Liu, L. Ma, Y. Wang, P. M. Ajayan, P. Nordlander, N. J. Halas, and F. J. Garcia de Abajo, ACS Nano **7**, 2388 (2013).
[23] Y. Hugen, X. Fengnian, L. Zhiqiang, and A. Phaedon, New J. Phys. **14**, 125001 (2012).
[24] D. B. Farmer, D. Rodrigo, T. Low, and P. Avouris, Nano Lett. **15**, 2582 (2015).
[25] C. M. Lieber, Nano Lett. **2**, 81 (2002).
[26] H. Yan, T. Low, W. Zhu, Y. Wu, M. Freitag, X. Li, F. Guinea, P. Avouris, and F. Xia, Nat. Photon **7**, 394 (2013).
[27] Y. Cao, X. Li, D. Wang, X. Fan, X. Lu, Z. Zhang, C. Zeng, and Z. Zhang, Phys. Rev. B **90**, 245415 (2014).
[28] A. Y. Nikitin, T. Low, and L. Martin-Moreno, Phys. Rev. B **90**, 041407 (2014).
[29] A. Y. Nikitin, F. Guinea, F. J. Garcia-Vidal, and L. Martin-Moreno, Phys. Rev. B **84**, 161407 (2011).
[30] Z. Fei, E. G. Iwinski, G. X. Ni, L. M. Zhang, W. Bao, A. S. Rodin, Y. Lee, M. Wagner, M. K. Liu, S. Dai, M. D. Goldflam, M. Thiemens, F. Keilmann, C. N. Lau, A. H. Castro-Neto, M. M. Fogler, and D. N. Basov, Nano Lett. **15**, 4973 (2015).
[31] S. Das Sarma and E. H. Hwang, Phys. Rev. Lett. **81**, 4216 (1998).
[32] J. Horng, C.-F. Chen, B. Geng, C. Girit, Y. Zhang, Z. Hao, H. A. Bechtel, M. Martin, A. Zettl, M. F. Crommie, Y. R. Shen, and F. Wang, Phys. Rev. B **83**, 165113 (2011).